Populations and lifetimes in the $v=n-\ell-1=2$ and 3 metastable cascades of $\bar{p}\mathrm{He}^+$ measured by pulsed and continuous antiproton beams

M. Hori, J. Eades, E. Widmann,* and T. Yamazaki†
CERN, CH-1211 Geneva 23, Switzerland

R. S. Hayano, T. Ishikawa, and H. A. Torii‡
Department of Physics, University of Tokyo, 7-3-1 Hongo, Bunkyo-ku, Tokyo 113-0033, Japan

T. von Egidy, F. J. Hartmann, B. Ketzer, C. Maierl, and R. Pohl§
Physik-Department, Technische Universität München, D-85747 Garching, Germany

M. Kumakura‖ and N. Morita
Institute for Molecular Science, Myodaiji, Okazaki 444-8585, Japan

D. Horváth
KFKI Research Institute for Particle and Nuclear Physics, H-1525 Budapest, Hungary

I. Sugai
High Energy Accelerator Research Organization (KEK), 1-1 Oho, Tsukuba, Ibaraki 305-0801, Japan
(Received 11 October 2003; published 26 July 2004)

The time evolution of the state populations in the $v\equiv n-\ell-1=2$ and 3 metastable cascades of antiprotonic helium ($\bar{p}^4\mathrm{He}^+$) atoms were studied using laser spectroscopy. The antiprotonic states $(n,\ell)=(39,35)$, (40,36), and (41,37) in the $v=3$ cascade were estimated to initially contain, respectively, $(0.28\pm0.04)\%$, $(0.06\pm0.02)\%$, and $(0.02\pm0.01)\%$ of the antiprotons stopped in the helium target, while the corresponding values for states (37,34), (38,35), and (39,36) in the $v=2$ cascade were $(0.21\pm0.04)\%$, $(0.49\pm0.07)\%$, and $(0.19\pm0.07)\%$. The shortening of the state lifetimes due to collisions between $\bar{p}\mathrm{He}^+$ and helium atoms was studied. As the atomic density of the target was increased from $\rho=2\times10^{20}$ to 2×10^{21} cm^{-3}, the lifetime of state (37,34) decreased by an order of magnitude, whereas the higher states (38,35) and (39,35) were relatively unaffected. Between densities $\rho=6\times10^{20}$ and 2×10^{22} cm^{-3}, a short-lived component with a time constant $\tau\sim0.2$ μs appeared at early times in the delayed annihilation time spectrum of $\bar{p}\mathrm{He}^+$, while the total fraction of long-lived antiprotons decreased from 3.0 to 2.5%. These effects were caused by the lifetime-shortening of specific $\bar{p}\mathrm{He}^+$ states such as (37,34).

DOI: 10.1103/PhysRevA.70.012504 PACS number(s): 36.10.Gv, 32.70.Cs, 34.90.+q

I. INTRODUCTION

When antiprotons are stopped in a helium target, a 3% fraction survive with an average lifetime $\tau_{\mathrm{avg}}=3-4$ μs [1–6] by forming metastable antiprotonic helium ($\bar{p}\mathrm{He}^+\equiv\bar{p}^-+\mathrm{He}^{2+}+e^-$) atoms [7,8]. In this paper, we study the initial distributions of these atoms over principal (n) and orbital angular momentum (ℓ) quantum numbers in the $v\equiv n-\ell-1=2$ and 3 metastable cascades using a laser spectroscopic method. The effect of collisions between $\bar{p}\mathrm{He}^+$ and ordinary helium atoms on the atomic cascade is also studied. The measurements were made using pulsed and continuous types of antiproton beam [9,10] supplied by the Low Energy Antiproton Ring (LEAR) of CERN. Although the experiments reported here ended in 1996 with the closure of LEAR, there is renewed interest in these unpublished data, in light of recent results [11,12] produced at CERN's Antiproton Decelerator (AD).

Experimental [12–19] and theoretical studies have shown that five phases can be discerned in the life history of metastable $\bar{p}\mathrm{He}^+$. (i) *Capture*: when an antiproton collides with a helium atom at electron-volt energies, it may replace one of the electrons orbiting the helium nucleus, and become captured into a $\bar{p}\mathrm{He}^+$ state. This occurs [12,20–28] with the highest probability into states with n-values of about

$$n\sim n_0\equiv\sqrt{M^*/m_e}=38.3 \tag{1}$$

(where M^* is the reduced mass of the antiproton-helium nucleus system, and m_e the electron mass), which corre-

*Present address: Department of Physics, University of Tokyo, 7-3-1 Hongo, Bunkyo-ku, Tokyo 113-0033, Japan.
†Present address: RI Beam Science Laboratory, RIKEN, Wako, Saitama 351-0198, Japan.
‡Present address: Institute of Physics, University of Tokyo, 3-8-1 Komaba, Meguro-ku, Tokyo 153-8902, Japan.
§Present address: Paul Scherrer Institut, 5232 Villigen PSI, Switzerland.
‖Present address: Department of Physics, Faculty of Science, Kyoto University, Kyoto 606-8502, Japan.

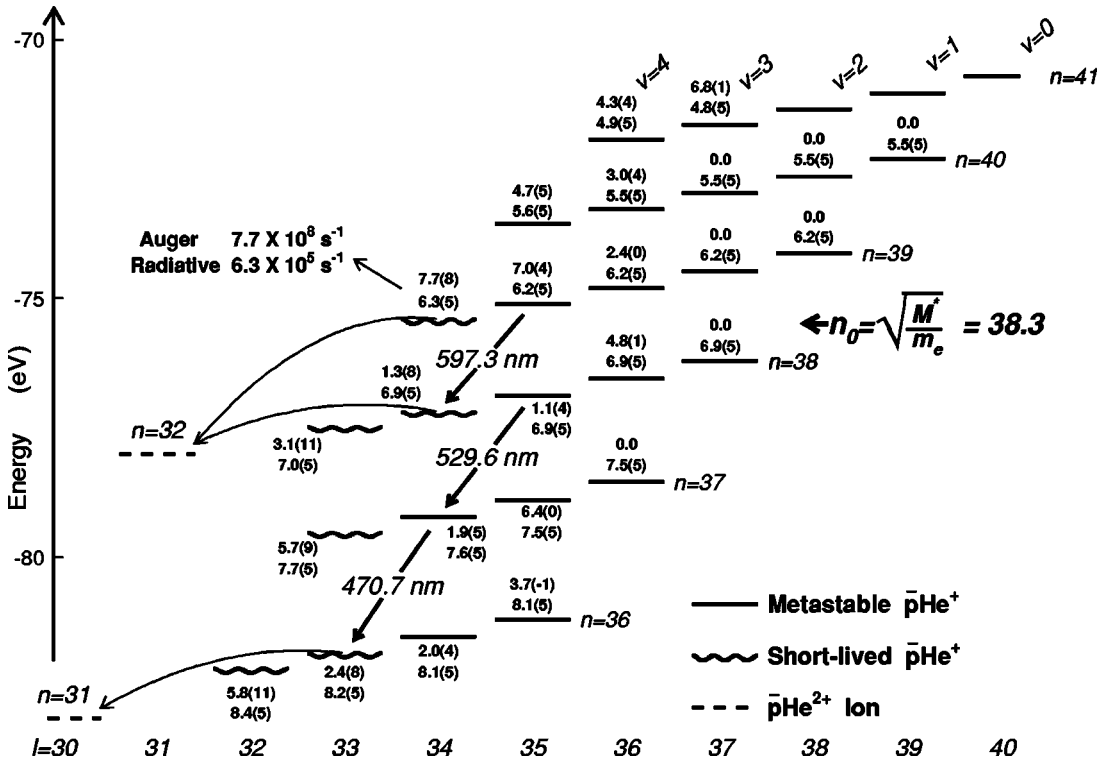

FIG. 1. Portion of the level structure of $\overline{p}^4\mathrm{He}^+$, with observed transition wavelengths shown in nanometers. The solid lines indicate radiation-dominated metastable states, the wavy lines Auger-dominated short-lived states. The theoretical values for Auger [22,33] and radiative transition [32] rates from some states (n,ℓ) are shown. The broken lines indicate $\overline{p}\mathrm{He}^{2+}$ ionic states formed after Auger emission, the curved arrows indicate Auger transitions with minimum $|\Delta\ell|$. On the left-hand scale the theoretical absolute energy of each state is plotted relative to the three-body breakup threshold.

sponds to an antiproton orbital with the same radius and binding energy as the displaced 1*s* electron. Auger emission of the second electron is suppressed for states with large ℓ values (Fig. 1) [7,8,29]. (ii) *Thermalization*: the $\overline{p}\mathrm{He}^+$ atom initially recoils with roughly the same momentum as the incoming antiproton, but cools down within picoseconds by colliding with the surrounding helium atoms. (iii) *Metastable cascade*: The antiproton cascades down through several metastable levels by making successive radiative transitions with lifetimes $\tau=1-2$ μs, these being primarily of the type $\Delta n=\Delta\ell=-1$ that keeps the vibrational quantum number $v\equiv n-\ell-1$ [30–32] constant. The states can therefore be grouped into the cascade sequences $v=0,1,2,3\ldots$. (iv) *Auger decay*: The antiproton finally reaches a short-lived state, from which Auger decay to an ionic state occurs within a few nanoseconds [8,22,33]. (v) *Stark mixing and annihilation*: the antiprotonic ℓ-levels in the daughter $\overline{p}\mathrm{He}^{2+}$ ion are degenerate, so that collisional Stark effects mix the antiprotonic states with the *S*, *P*, and *D* states at high *n*, causing immediate annihilation [34,35]. The consequence of the above sequence of events is that the measured lifetime of antiprotons exhibits a slowly decaying component in the delayed annihilation time spectrum, extending for several microseconds from the instant they were stopped in the helium target.

Laser spectroscopic studies of the primary populations $P_{(n,\ell)}(t=0)$ [i.e., the number of antiprotons populating a state (n,ℓ) at atomic formation, normalized to the total number of antiprotons stopped in the target] and lifetimes of $\overline{p}\mathrm{He}^+$ were started at LEAR [13–17], which delivered antiprotons as either a single high-intensity pulse containing $3\times10^7-1\times10^9$ antiprotons and lasting $\Delta t\sim200-300$ ns, or as a continuous, low-intensity beam at rates $\sim10^4$ $\overline{p}$/s. Metastable $\overline{p}\mathrm{He}^+$ atoms were produced by stopping either variety of beam in a helium target. They were irradiated with a resonant laser pulse, which induced antiproton transitions between adjacent pairs of metastable and short-lived $\overline{p}\mathrm{He}^+$ states (Fig. 1). This forced the immediate annihilation of antiprotons populating the metastable state, thereby producing a sharp spike in the delayed annihilation time spectrum. In the example spectrum shown in Figs. 2(a) and 2(b) measured using, respectively, the pulsed and continuous types of antiproton beam, the laser transition $(n,\ell)=(39,35)\rightarrow(38,34)$ at wavelength $\lambda=597.3$ nm was induced at $t=1.6$ μs. The intensity of the annihilation spike was proportional to the population $P_{(39,35)}(t)$ in the parent state at *t*. By adjusting the timing of the laser pulse between $t=0.3$ and 10 μs, the time evolution of $P_{(39,35)}(t)$ was measured, from which the primary population $P_{(39,35)}(t=0)$ was estimated by extrapolating the data to $t=0$.

Both types of antiproton beam had advantages and disadvantages; in experiments using the pulsed antiproton beam [36], large numbers of $\overline{p}\mathrm{He}^+$ were produced simultaneously in a way which allowed the state populations at very early times ($t=0.3$ μs) to be studied [11,12]. The spectra, however, contained a large background caused by delayed

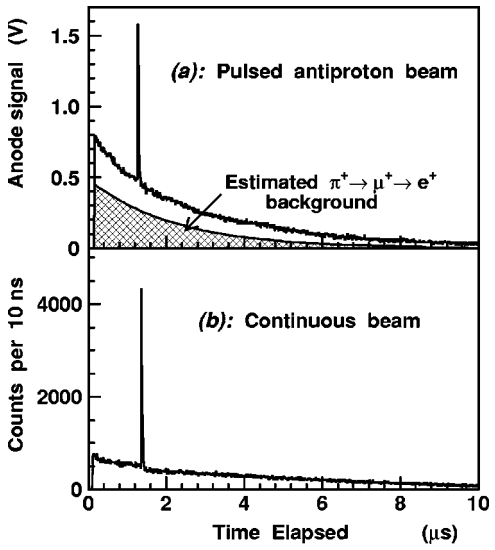

FIG. 2. Delayed annihilation time spectrum measured using a pulsed antiproton beam, with the resonance transition $(n,\ell)=(39,35)\rightarrow(38,34)$ at wavelength $\lambda=597.3$ nm induced at $t=1.6$ μs (a). The hatched area represents the estimated contribution of $\pi^+\rightarrow\mu^+\rightarrow e^+$ decay. The background-free spectrum was measured using a continuous antiproton beam at the same target conditions, the spike was induced at the same timing (b).

positrons (i.e., those produced by $\pi^+\rightarrow\mu^+\rightarrow e^+$ decay) [36], which could not be eliminated or accurately quantified due to the analog nature of the measurement (see Sec. II). This made it difficult to estimate the absolute number of antiprotons populating the $\bar{p}\mathrm{He}^+$ states, normalized to the total number of stopped antiprotons. In experiments using the continuous antiproton beam, $\bar{p}\mathrm{He}^+$ were produced in an event-by-event manner, allowing the antiprotons occupying individual metastable states to be accurately counted under background-free conditions. Due to technical reasons (see Sec. II), however, the laser could not be fired at time regions $t<1.6-1.8$ μs [14]. We therefore used the pulsed antiproton beam to measure the relative values of the populations at early times, then relied on spectra obtained using the continuous beam to correctly normalize them.

We recently used the AD to study the primary populations of 20 metastable states in the isotopes $\bar{p}^4\mathrm{He}$ and $\bar{p}^3\mathrm{He}$ [12]. The region $n=37-40$ accounted for nearly all of the observed 3% fraction of antiprotons captured into metastable states, which agreed with the estimation of Eq. (1). Unlike LEAR, however, the AD can produce only a pulsed antiproton beam, with a significant $\pi^+\rightarrow\mu^+\rightarrow e^+$ background in the measured $\bar{p}\mathrm{He}^+$ spectra. The work of Ref. [12], therefore, critically depended on comparisons with the data and analysis reported here to obtain accurate values on the primary populations.

In a previous paper [17], the shortening of the state lifetimes caused by collisions between $\bar{p}\mathrm{He}^+$ and helium atoms was studied. State $(39,35)$ had a lifetime $\tau_{(39,35)}=1.5\pm0.1$ μs, which was relatively unchanged between atomic densities of the helium target $\rho=2\times10^{20}$ and 1.9×10^{22} cm^{-3}. In contrast, the lifetime of state $(37,34)$

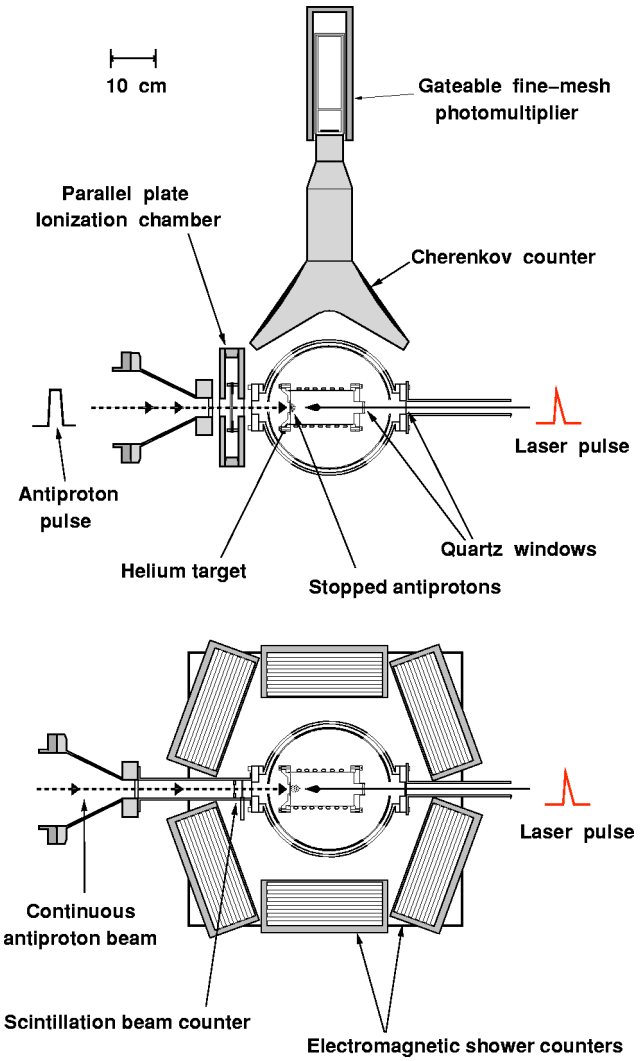

FIG. 3. Schematic layout of the experiments using pulsed (top) and continuous (bottom) antiproton beams.

decreased from $\tau_{(37,34)}=1.2$ μs at $\rho=1\times10^{20}$ cm^{-3} to 0.13 μs at 5.8×10^{21} cm^{-3}. In the present work, we measured the effect of collisions on the population evolution of states in the $v=2$ and 3 cascades, at densities between $\rho=2\times10^{20}$ and 1.2×10^{22} cm^{-3}. Systematic measurements of the delayed annihilation time spectrum undisturbed by laser irradiation were also made at densities $\rho=6\times10^{20}-2\times10^{22}$ cm^{-3}.

The deduction and normalization of the primary populations is a complicated task, but it has been done and presented here. The paper is organized in the following way. Section II describes the laser spectroscopy experiments of $\bar{p}\mathrm{He}^+$ using pulsed and continuous antiproton beams in some detail. Precise measurements of populations depend on a variety of factors, the estimations of which are presented in Sec. III. The experimental data on the $v=2$ and 3 metastable cascades of $\bar{p}\mathrm{He}^+$ are described in Sec. IV. Finally, some discussions and conclusions are given in Secs. V and VI.

II. EXPERIMENTAL METHOD

A. Experiments using a pulsed antiproton beam

In Fig. 3 (upper half), the experimental layout wherein 200–300-ns-long pulses containing between 3×10^7 and 1×10^9 antiprotons with kinetic energy $E=21$ MeV were injected into a cryogenic helium target is shown [36]. The intensity, time structure, and *XY* profile of these pulses were measured by a parallel plate ionization chamber [37] placed in the beam upstream of the target. The target [17] was a 150-mm-long, 70-mm-diam stainless-steel cylinder, into which the antiprotons entered through a 0.5-mm-thick copper-beryllium window. A 20-mm-diam quartz window was affixed to the opposite end of the chamber to admit the laser beam. Measurements were made using helium gas at pressures $P=0.1$–3.5 bar and temperatures $T=5.8$–6.6 K. Hereafter we express each target condition in atomic density ρ (in cm^{-3}), pressure P (in bar), and temperature T (in degrees Kelvin).

Some 97% of the antiprotons annihilated promptly after stopping in the helium, whereas 3% of them formed between 1×10^6 and 3×10^7 metastable $\bar{p}\mathrm{He}^+$ atoms with an average lifetime $\tau_{\mathrm{avg}}=3$–4 μs against annihilation. The charged pions emerging from these annihilations produced Cherenkov light in 2-cm-thick acrylic detectors placed around the target [36]. Neutral pions also emerged, and decayed into γ-ray pairs with a lifetime $\tau=0.08$ fs [38]. An estimated 30% of the γ rays converted into electron and positron pairs while traveling through the target walls, and these also produced Cherenkov light in the acrylic plates. The rate of annihilations was so high that individual particles could not be resolved. Instead, the Cherenkov detector produced a single continuous light pulse consisting of an extremely bright, 200–300-ns-long flash from the promptly annihilating antiprotons, followed by a much longer ($\Delta t\sim20$ μs) but less intense tail from delayed annihilations of the metastable $\bar{p}\mathrm{He}^+$. This light envelope was detected by a gateable fine-mesh photomultiplier [36], and the analog wave form of the anode signal was recorded by a digital oscilloscope [Fig. 2(a)]. The photomultiplier was deactivated during the initial flash, in order to suppress the strong burst of photoelectrons which would otherwise saturate the detector or produce spurious afterpulse signals [36]. Due to this gating, however, information about the prompt annihilation could not be obtained. Afterwards the detector was reactivated so that the delayed annihilation was observed starting from $t\sim0.2$ μs. The spectrum contained a strong background with a time constant $\tau\sim2$ μs, produced in the following way: (i) the low-energy π^+-mesons emerging from the annihilations stopped in the target walls or in the detector, (ii) these decayed into positive muons with a lifetime $\tau=26$ ns [38], and further decayed into positrons with a lifetime $\tau=2.2$ μs and average energy $E=40$ MeV, (iii) some of these positrons struck the detector and produced delayed Cherenkov photons. This background could not be distinguished from the signal produced by the metastable atoms, which contained multiple decay components with lifetimes $\tau=0.2$–5 μs. The π^--mesons did not produce a long-lived background, since they formed π^- atoms and were absorbed immediately by the atomic nuclei [39].

The metastable atoms were irradiated by laser pulses fired into the target, collinear with the antiproton beam but in the opposite direction. Two sets of dye lasers pumped by XeCl excimer lasers were used to produce 15-mm-diam, 40-ns-long laser pulses with bandwidths $\Gamma\sim6$ GHz and energy densities $\Theta\sim1$ $\mathrm{mJ/cm}^2$. By independently adjusting the timings of the two lasers relative to the arrival time of the antiprotons, $\bar{p}\mathrm{He}^+$ transitions were induced at various times between $t=0.3$ and 10 μs. The transition wavelengths shifted by 1–10 GHz [11,19] as the target density was increased, and so the laser wavelength was corrected for this shift.

B. Experiments using a continuous antiproton beam

The layout of the experiment using a continuous antiproton beam is shown in Fig. 3 (lower half) [13,17,40]. Antiprotons were injected into the target at a rate $f\sim10^4$ s^{-1}. Since the metastable $\bar{p}\mathrm{He}^+$ annihilated with an average lifetime $\tau_{\mathrm{avg}}=3$–4 μs, only one atom existed in the target at a time. The arrival of each antiproton was detected by a 0.5-mm-thick plastic scintillation beam counter positioned upstream of the target. Its annihilation was identified with $99.7\pm0.1\%$ efficiency by seven shower counters surrounding the target. The annihilation time was thus measured relative to the time of passage of the antiproton through the beam counter. The background due to $\pi^+\rightarrow\mu^+\rightarrow e^+$ decay was rejected by requiring the simultaneous detection of at least two pions produced in an annihilation event [40]. In this way, a background-free spectrum containing 10^6–10^8 events which showed both the prompt and delayed annihilations was obtained [4,6]. The laser pulses reached the target at $t=1.6$ μs [Fig. 2(b)] or later, this being the minimum delay achievable by the method of identifying the randomly occurring metastable events, and then triggering the excimer lasers.

III. ESTIMATION OF THE PRIMARY POPULATIONS

A. General method

The primary populations $P_{(n,\ell)}(t)$ were estimated using the following formulas,

$$P_{(n,\ell)}(t)=\frac{If_{\mathrm{trap}}}{\varepsilon f_{\mathrm{stop}}(1-f_{\mathrm{back}})}, \tag{2a}$$

$$f_{\mathrm{trap}}=\frac{f_{\mathrm{delayed}}}{(1-f_{\mathrm{nuc}})}, \tag{2b}$$

the variables being (i) f_{trap}: the probability of a stopped antiproton forming a metastable atom and surviving more than 20 ns, (ii) f_{delayed}: the number of delayed events (those appearing later than $t=20$ ns in the delayed annihilation time spectrum) normalized to the total number of annihilations, (iii) f_{nuc}: the probability of an antiproton undergoing an in-flight nuclear reaction and annihilating, (iv) I: the measured intensity of the laser-induced annihilation spike, normalized to the total number of delayed annihilations, (v) ε: the efficiency of the laser pulse depleting the metastable population in the resonance parent state, (vi) f_{stop}: the probability of an antiproton stopping in the volume of the helium target irra-

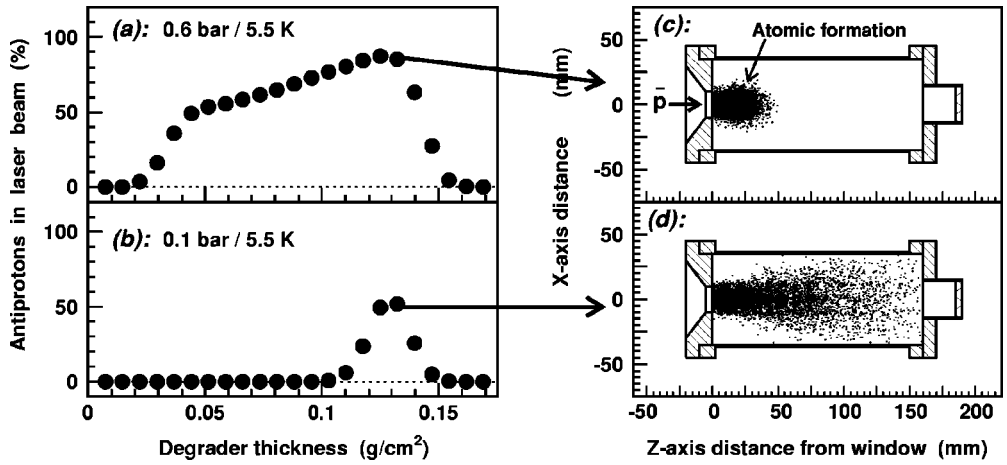

FIG. 4. Estimated ratios of antiprotons stopping in the volume of the helium target irradiated by the laser beam, as a function of polyimide degrader thickness (a),(b). A two-dimensional projection of the target chamber, showing the spatial distribution of the stopped antiprotons at two target densities, and the degrader thicknesses indicated by the arrows (c),(d).

diated by the laser, (vii) $f_{\rm back}$: the contribution of background events in the delayed annihilation time spectrum caused by $\pi^+ \rightarrow \mu^+ \rightarrow e^+$ decay. In the proceeding subsections, we will discuss these factors and estimate their values.

B. Estimations of stopping distributions and in-flight nuclear reactions

A Monte Carlo simulation of antiprotons slowing down and stopping in the helium target was made, using the experimental values for the energy loss [41,42] and including the multiple scattering effect according to the Moliere distribution, and the energy straggling effect according to the Vavilov distribution. The antiproton beam passing through the copper-beryllium window was estimated to have a large emittance ($\Xi > 500\pi$ mm mrad), kinetic energy distribution ($E=1-2$ MeV), and diameter ($d=8-10$ mm), so that they stopped in a relatively large volume in the helium depending on the target density. The average energy of the antiprotons emitted from the window was adjusted by varying the thickness t_d of polyimide (Ube Industries Upilex-S) degrader foils inserted in the beam upstream of the target; the fraction $f_{\rm stop}$ of antiprotons stopping in the volume of helium gas irradiated by the 15-mm-diam collinear laser beam, to the total number of stopped antiprotons, was thus maximized. In Fig. 4(a), the simulated dependence of $f_{\rm stop}$ on t_d is shown at a target density $\rho=9\times10^{20}$ cm^{-3} ($P=0.6$ bar, $T=5.5$ K); the maximum value $f_{\rm stop}\sim90\%$ was obtained at $t_d=0.13$ g/cm^2, the corresponding stopping distribution of which is shown in Fig. 4(c). At a lower density $\rho=1.3\times10^{20}$ cm^{-1} ($P=0.1$ bar, $T=5.5$ K), however, $f_{\rm stop}$ reached a maximum value of only 50–60% [Figs. 4(b) and 4(d)]. At even lower densities, most of the antiprotons stopped in the walls at the opposite end of the target, so that laser spectroscopic signals of $\overline{p}$He$^+$ could no longer be observed.

During the experiment, the degrader thickness t_d was adjusted so as to maximize the intensity of the laser-induced annihilation spike appearing in the delayed annihilation time spectrum (Fig. 2). This experimentally-optimized thickness t_d was within ±0.01 g/cm^2 of the value predicted by the above simulation. Slightly smaller values of t_d were used during measurements of $\overline{p}$He$^+$ time spectra undisturbed by the laser irradiation (see proceeding subsection), thereby ensuring that very few antiprotons annihilated in the entrance window of the target.

The fraction $f_{\rm nuc}$ of antiprotons that underwent in-flight nuclear reactions (i.e., high-energy antiprotons colliding with the atomic nuclei and annihilating) in the beam detector, degrader foil, copper-beryllium window, or helium gas was also estimated in the above Monte Carlo simulation. We tracked the trajectories of 10^6 simulated antiprotons fired into a helium target of density $\rho=9\times10^{20}$ cm^{-3} ($P=0.6$ bar, $T=5.5$ K), until they stopped or annihilated in-flight. The simulation used the following cross-sections $\sigma_{\rm an}$ of antiproton annihilation on various target nuclei; (i) *hydrogen*: the experimental cross section of the $\overline{p}+p$ reaction measured at antiproton momenta between $p=40$ and 200 MeV/c [43] were utilized, whereas theoretical values [44,45] were used

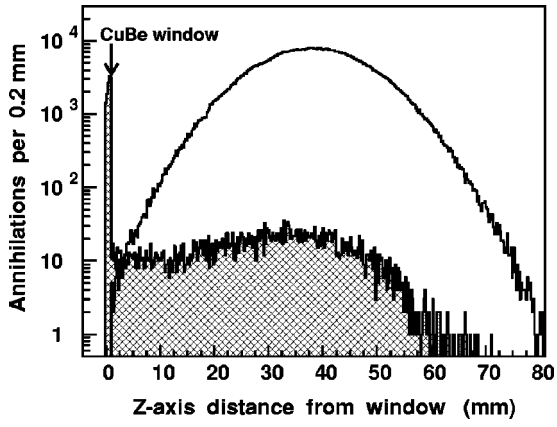

FIG. 5. The simulated range curve of annihilation events along the longitudinal direction of the antiproton beam. Some 3% of the antiprotons annihilate in nuclear reactions in-flight, the contribution of which is shown by the hatched area. The unshaded area represents antiprotons that form atoms.

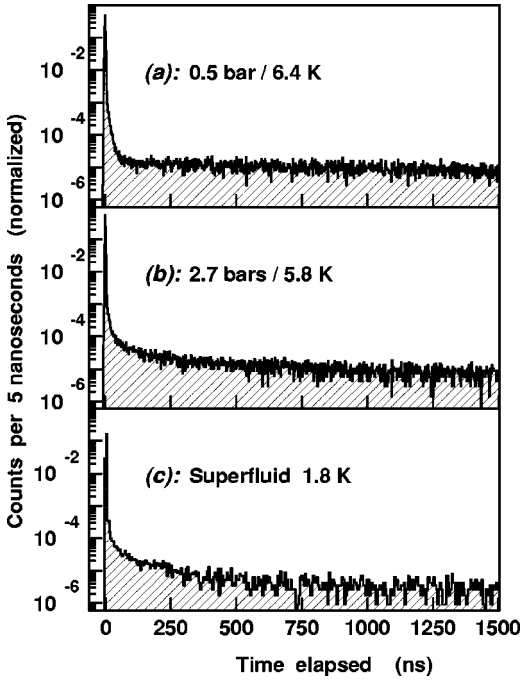

FIG. 6. Delayed annihilation time spectra, measured at a target pressure $P=0.5$ bar and temperature $T=6.4$ K (a), $P=2.7$ bar and $T=5.8$ K (b), and a superfluid target at $T=1.8$ K (c).

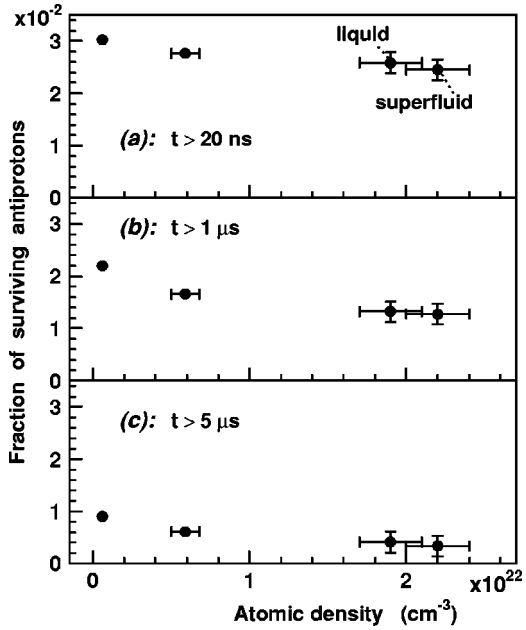

FIG. 7. The fractions of antiprotons surviving more than 20 ns (a), 1 μs (b), and 5 μs (c) at various densities of the helium target.

at $p<40$ MeV/c where no experimental data exists, (ii) *helium*: experimental σ_{an} values at momenta $p=50-70$ MeV/c [46], and theoretical values [45] at lower and higher momenta were used, (iii) *heavier nuclei*: the cross sections of antiproton annihilation on nuclei of atomic number $A>10$ at momenta $p=0-200$ MeV/c were estimated by an unified optical model [47,48]. The σ_{an} values of the reaction $\bar{p}$+Ne obtained from this model agreed with experimental data measured at $p=60-190$ MeV/c [49,50]. We thus assumed in the simulation that as the antiprotons decelerated from $p=200$ to 20 MeV/c, the cross sections for the annihilation reactions $\bar{p}$+He, $\bar{p}$+C, and $\bar{p}$+Cu, respectively, increased from $\sigma_{an}=0.4$ to 3 b, 0.7 to 6 b, and 2 to $\sim$40 b. In Fig. 5, the range curve of annihilations along the longitudinal direction of the antiproton beam due to in-flight reactions (represented by the hatched area), and those due to $\bar{p}$He$^+$ atomic formation (unshaded area) are compared. Of the 10^6 simulated antiprotons, an estimated $f_{nuc}\sim 3\%$ underwent in-flight reactions, most of these occurring in the degrader foil and copper-beryllium window which appear as a sharp spike near $z=0$ mm. The simulation may be unreliable at very low antiproton energies, particularly in the sub-keV region where the cross section of atomic formation becomes larger than σ_{an}.

C. Total yield f_{trap} of metastable $\bar{p}$He$^+$ atoms

We next measured the fraction of metastable atoms f_{trap} produced per stopped antiproton. In Figs. 6(a)–6(c), delayed annihilation time spectra measured at three target densities using the continuous antiproton beam are shown. At a density $\rho=6\times10^{20}$ cm^{-3} ($P=0.5$ bar, $T=6.4$ K), the spectrum showed a 10–20-ns-wide prompt annihilation peak containing 97% of the antiprotons, and a long-lived component decaying with an average lifetime $\tau_{avg}=4$ μs. In superfluid helium at a temperature $T=1.8$ K (corresponding to a density $\rho=2\times10^{22}$ cm^{-3}) [51], a larger fraction of antiprotons annihilated at early times, causing a short-lived component with a lifetime $\tau_{short}=0.2$ μs to appear.

In Fig. 7(a) and Table I, the fraction f_{trap} of antiprotons surviving more than $t_{meta}=20$ ns after stopping are presented

TABLE I. Fractions of antiprotons surviving more than 20 ns, 1 μs, and 5 μs in helium targets at various densities.

Density		Pressure	Temperature	Antiprotons survived after t_{meta} (%)		
(10^{20} cm^{-3})	Phase	(bar)	(K)	$t_{meta}>20$ ns	$t_{meta}>1$ μs	$t_{meta}>5$ μs
0.59±0.06	Gas	0.50±0.01	6.4±0.2	3.0±0.1	2.2±0.1	0.9±0.1
5.9±0.9	Gas	2.70±0.05	5.8±0.2	2.8±0.1	1.7±0.1	0.6±0.1
19±2	Liquid		4.2±0.1	2.6±0.1	1.3±0.1	0.4±0.1
22±2	Superfluid		1.8±0.1	2.5±0.1	1.3±0.1	0.3±0.1

as a function of target density. These values have been corrected for the $f_{\mathrm{nuc}}\sim 3\%$ background caused by in-flight nuclear reactions. The arbitrary choice of $t_{\mathrm{meta}}=20$ ns to define metastability is a matter of convenience only; indeed, values of $t_{\mathrm{meta}}=15$ ns [6] and 20 ns [4] have been used in past publications. The present analysis was made in a way such that the estimated values for the primary populations $P_{(n,\ell)}(t=0)$ did not depend on the t_{meta} value chosen above. As the density was increased from $\rho=6\times10^{20}$ to 2×10^{22} cm^{-3}, the fraction f_{trap} decreased from $(3.0\pm0.1)\%$ to $(2.5\pm0.1)\%$. In the same density range, the atoms that survived more than 1 μs and 5 μs [Figs. 7(b) and 7(c)] respectively decreased from $f_{t>1\ \mu\mathrm{s}}=(2.2\pm0.1)\%$ to $(1.3\pm0.1)\%$, and from $f_{t>5\ \mu\mathrm{s}}=(0.9\pm0.1)\%$ to $(0.3\pm0.1)\%$. This shows that collisions between $\bar{p}\mathrm{He}^+$ and helium atoms affect the delayed annihilation time spectrum in both nanosecond- and microsecond-scale time ranges.

D. Estimation of the depletion efficiency ε

The efficiency ε of the laser pulse depleting the population $P_{(n,\ell)}(t)$ in the parent state of the transition $(n,\ell)\rightarrow(n',\ell')$ [i.e. $\varepsilon=1$ if the laser induces all the antiprotons occupying (n,ℓ) to annihilate, and $\varepsilon=0$ when no such annihilations occur] was estimated from theoretical calculations. Generally, large values of ε are attained if two conditions are met: (i) the energy of the laser pulse is high enough to induce many Rabi oscillations within its duration $\Delta t_{\mathrm{laser}}=40$ ns, (ii) the lifetime $\tau_{(n',\ell')}$ of the daughter state is short compared to $\Delta t_{\mathrm{laser}}$. In Fig. 8(a), a typical time profile of the laser pulse measured using a *p-i-n* photodiode is shown. It has a two-peak structure with a sharp peak in the first 10 ns. In Fig. 8(b), an experimentally observed annihilation spike corresponding to the transition $(39,35)\rightarrow(38,34)$ at wavelength $\lambda=597.3$ nm is shown. The dotted line represents the theoretical profile obtained by integrating the optical Bloch equation,

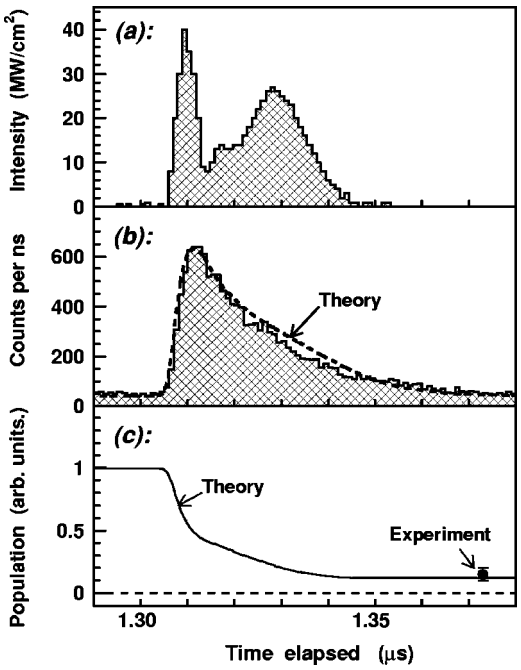

FIG. 8. Typical temporal profile of the laser pulse with an energy density $\Theta=1$ mJ/cm^2 (a). Experimental (solid line) and theoretical (dotted line) profiles of the 597.3-nm resonance spike (b). The simulated population evolution of the resonance parent state $(n,\ell)=(39,35)$ during the laser pulse (solid line), and the measured depopulation efficiency (closed circle) (c).

$$\frac{d}{dt}\begin{pmatrix}P_{1m}\\P_{2m}\\P_{xm}\\P_{ym}\end{pmatrix}=\begin{pmatrix}-1/\tau_{1m} & 0 & 0 & \Omega_m(t)/2\\ 0 & -1/\tau_{2m} & 0 & -\Omega_m(t)/2\\ 0 & 0 & -(1/\tau_{1m}+1/\tau_{2m})/2-\Gamma_m & \Delta\omega\\ -\Omega_m(t) & \Omega_m(t) & -\Delta\omega & -(1/\tau_{1m}+1/\tau_{2m})/2-\Gamma_m\end{pmatrix}\begin{pmatrix}P_{1m}\\P_{2m}\\P_{xm}\\P_{ym}\end{pmatrix}, \tag{3}$$

where the populations in the resonant parent and daughter states with a magnetic quantum number m are denoted by P_{1m} and P_{2m}, and the real and imaginary parts of the off-diagonal terms in the density matrix by P_{xm} and P_{ym}. The state lifetimes are denoted by τ_{1m} and τ_{2m}, and the detuning of the laser from the transition frequency by $\Delta\omega$. The rate of dephasing collisions Γ_m was estimated to be less than 0.5 GHz at the typical target densities studied here, based on separate measurements of the $\bar{p}\mathrm{He}^+$ resonance profile. The frequency $\Omega_m(t)/2\pi$ (in gigahertz) of Rabi oscillations between two states (n,ℓ,m) and $(n\pm1,\ell-1,m)$ induced by a linearly-polarized laser pulse with a time profile $\Theta(t)$ [in kilowatts per cm^2, see Fig. 8(a)] can be calculated as

$$\frac{\Omega_m(t)}{2\pi}=0.44\mu\sqrt{\Theta(t)\frac{(\ell-m-1)(\ell+m-1)}{\ell(2\ell-1)}}. \tag{4}$$

The dipole moment μ (in Debye) of the transition was derived using its spontaneous radiative rate $1/\tau$ (in hertz) and wavelength λ (in meters) as

$$\mu=1.8\sqrt{\frac{\lambda^3}{\tau}}\times10^6, \tag{5}$$

the relevant values being 0.62 D, 5.5×10^5 Hz, and 5.973×10^{-7} m. After numerically integrating Eq. (3) and averaging over m, the resulting profile was convoluted with a

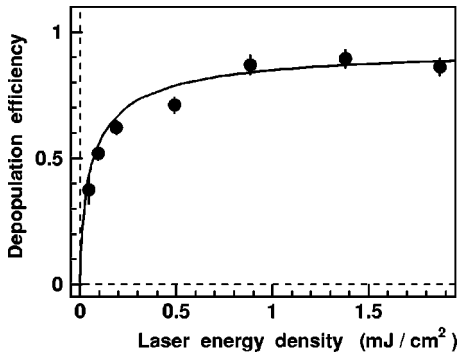

FIG. 9. Experimental (closed circles) and theoretical (solid line) depletion efficiencies of the laser pulse tuned to the transition $(39,35)\rightarrow(38,34)$ at wavelength $\lambda=597.3$ nm at various energy densities of the laser.

Gaussian having a full-width-at-half-maximum of 6 GHz, to simulate the effects caused by the finite laser bandwidth.

In Fig. 8(c), the simulated time evolution of the population in state (39,35) during irradiation with the laser pulse [Fig. 8(a)] is shown. The depletion efficiency was estimated to be $\varepsilon=90\%$. This agreed with the value (indicated by the closed circle with error bar) measured in a separate experiment wherein the $\bar{p}\mathrm{He}^+$ was irradiated with two successive laser pulses (see Sec. IV). In Fig. 9, experimental values of ε (plotted using closed circles) measured at various energy densities of the laser between $\Theta=0.05$ and 2 mJ/cm^2 are shown. These were in good agreement with the theoretical values (solid line) estimated above using Eq. (3). The population measurements described below were all carried out at an energy density $\Theta>1$ mJ/cm^2 where the spike intensity was maximized and ε saturated at a value of $\sim$90%.

E. Intensities of the laser-induced annihilation spikes

We now return to Fig. 2(a), which shows the delayed annihilation time spectrum measured by injecting a 200–300 ns-long beam pulse containing 1×10^8 antiprotons into a helium target at a density $\rho=8\times10^{20}$ cm^{-3} ($P=0.6$ bar, $T=5.8$ K). The laser transition $(39,35)\rightarrow(38,34)$ at a wavelength $\lambda=597.3$ nm is induced at $t=1.6$ μs in the spectrum. As described in Sec. I, we cannot determine the population of state (39,35) from this spectrum alone, because a fraction f_{back} of it is background due to $\pi^+\rightarrow\mu^+\rightarrow e^+$ decay.

In Fig. 2(b), the spectrum measured using the continuous antiproton beam at the same target conditions is shown, with the 597.3-nm transition induced at the same timing. This spectrum is background-free (i.e., $f_{\mathrm{back}}=0$), so that a precise count of $\bar{p}\mathrm{He}^+$ atoms can be obtained. The spike intensity I was derived by counting the number of annihilations under the spike, and normalizing to the total number of delayed annihilations. Using (i) the measured value of f_{trap}, (ii) the values ε and f_{stop} estimated from the above simulations, and (iii) Eq. (2), the population in state (39,35) at $t=1.6$ μs was estimated to be $P_{(39,35)}(t=1.6\ \mu\mathrm{s})=(0.12\pm0.02)\%$.

F. Estimation of the $\pi^+\rightarrow\mu^+\rightarrow e^+$ background

To estimate the contribution f_{back} of the $\pi^+\rightarrow\mu^+\rightarrow e^+$ background appearing in the spectrum of Fig. 2(a), a Monte Carlo simulation [36] was made using the GEANT version 4 program [52]. Computer models of the cryogenic target, Cherenkov detector, and surrounding material were generated. Each simulated annihilation produced secondary particles with experimentally known branching ratios and multiplicites. On average 1.5 π^+-mesons, 1.8 π^--mesons, and ~2 π^0-mesons were produced per $\bar{p}+{}^4\mathrm{He}$ reaction, although in $\sim$5% of the cases, more than seven mesons emerged [36]. To simulate the momentum distributions of these particles (with rest masses M_i), a simplified model was used where the kinetic energy $E-\Sigma_i M_i$ produced in the annihilation ($E=1.9$ GeV being the total energy of a $\bar{p}+p$ or $\bar{p}+n$ reaction) was distributed among them assuming a relativistic phase-space distribution. The momentum distribution of π^-'s simulated in this way [36] was found to agree with the experimental data for antiprotons annihilating on ^{4}He nuclei [53] in the momentum region $p=0.15-0.9$ GeV/c, both distributions showing maxima around $p=0.25$ MeV/c.

The trajectories of all the particles were followed until $t=15$ μs. The important decay and reaction processes were simulated, such as $\pi^\pm\rightarrow\mu^\pm\rightarrow e^\pm$ and $\pi^0\rightarrow2\gamma$ decays, multiple scattering, ionization, bremsstrahlung, e^+e^- annihilation and pair creation. The creation and propagation of the Cherenkov photons inside the detector was simulated, taking into account the optical attenuation, reflection, and scattering inside the radiator material. The quantum efficiency and time response of the photomultiplier was measured, and their effects were included into the simulation. The actual number of photoelectrons produced by the Cherenkov counter per incident particle was measured in a calibration experiment carried out at the 1.3 GeV electron synchrotron at KEK-Tanashi [36], and the data used to correct the simulation. Some $f_{\mathrm{trap}}=50-60\%$ of the analog spectrum [Fig. 2(a), hatched area] was attributed to $\pi^+\rightarrow\mu^+\rightarrow e^+$ decay.

A separate estimation on the $\pi^+\rightarrow\mu^+\rightarrow e^+$ yield was made by comparing the intensity of the laser-induced annihilation spike in Fig. 2(a) with that appearing in the background-free spectrum of Fig. 2(b) measured using the continuous antiproton beam. Due to the presence of the $\pi^+\rightarrow\mu^+\rightarrow e^+$ background, the relative intensity of the former spike was found to be smaller than the later spike by an amount which was compatible with the value 50–60% for f_{trap} estimated by the above simulation.

IV. EXPERIMENTAL RESULTS

A. Population evolution of metastable states in the $v=3$ cascade

The population in the last metastable state $(n,\ell)=(39,35)$ in the $v=3$ cascade was measured by inducing the transition $(39,35)\rightarrow(38,34)$ at wavelength $\lambda=597.3$ nm, at various times between $t=0.3$ and 10 μs as shown in Figs. 10(a)–10(c). At a target density $\rho=6\times10^{20}$ cm^{-3} ($P=0.5$ bar, $T=6.4$ K), the population decayed as a single exponential with a lifetime $\tau_{\mathrm{avg}}=1.9\pm0.1$ μs [Fig. 10(d)]. This represented the cumulative effect of the lifetime $\tau_{(39,35)}$ of state (39,35), and the feeding from the higher state (40,36) in the cascade. Extrapolation to time zero yielded a primary

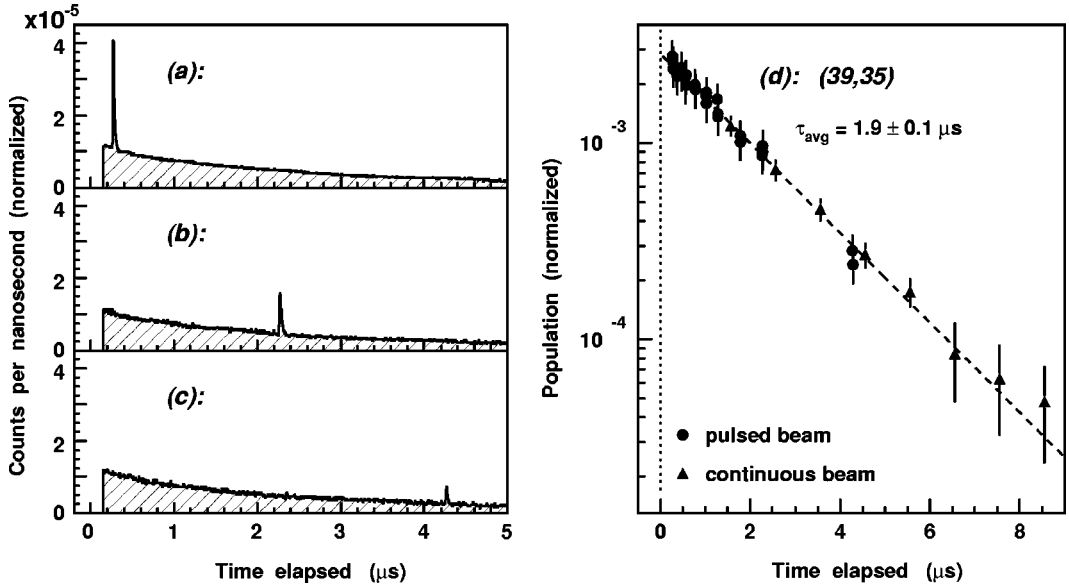

FIG. 10. Delayed annihilation time spectra measured using the pulsed antiproton beam, the resonance transition $(n,\ell)=(39,35)\rightarrow(38,34)$ at wavelength $\lambda=597.3$ nm induced at $t=0.3$ μs (a), 2.3 μs (b), and 4.3 μs (c). The population evolution of state (39,35) was measured using the pulsed (closed circles) and continuous (triangles) antiproton beams (d). All data were measured at a target pressure $P=0.5$ bar and temperature $T=5.8$ K.

population of $P_{(39,35)}(t=0)\sim 0.2\%$. The population and lifetime were relatively unaffected at densities between $\rho=2\times10^{20}$ and 1×10^{22} cm^{-3}.

To derive the populations in states (40,36), (41,37), and above in the $v=3$ cascade (Fig. 1), each atom was irradiated with two successive laser pulses tuned to the 597.3-nm transition, at independently varying times t_1 and t_2 [14]. In Figs. 11(a)–11(c), the spectra measured with the first laser fixed at $t_1=1.6$ μs while the second laser was scanned over three different timings $t_2=1.8$, 2.6, and 5.6 μs are shown. Now the number of annihilation counts in the first laser spike is equal to $\varepsilon P_{(39,35)}(t_1)$, so that the population remaining in state (39,35) after laser irradiation is equal to $(1-\varepsilon)P_{(39,35)}(t_1)$. The state is then refilled by spontaneous feeding from (40,36), the contribution of which can be determined by measuring the number of annihilations induced by the second laser at t_2.

In Figs. 11(d)–11(g), the recovery of the population measured by the second laser pulse is shown (represented by closed circles), for cases where the first laser (closed squares) was fired at $t_1=1.6$, 2.6, 3.6, and 4.6 μs. All these data points [including the population evolution measured using a single laser pulse shown in Fig. 11(h)] were simultaneously fit with a cascade model describing a three-level sequence of $\Delta n=\Delta\ell=-1$ transitions with population changes

$$dP_{(41,37)}=-\frac{P_{(41,37)}}{\tau_{(41,37)}}dt, \tag{6a}$$

$$dP_{(40,36)}=\left(-\frac{P_{(40,36)}}{\tau_{(40,36)}}+\frac{P_{(41,37)}}{\tau_{(41,37)}}\right)dt, \tag{6b}$$

$$dP_{(39,35)}=\left(-\frac{P_{(39,35)}}{\tau_{(39,35)}}+\frac{P_{(40,36)}}{\tau_{(40,36)}}\right)dt. \tag{6c}$$

Of course, there are also contributions from Auger decay and radiative processes that change $v\equiv n-l-1$, but calculations for a single isolated atom suggest that these contributions are all less than 10% [22,30–32]. According to this model, the intensity $I_1(t_1)$ of the first spike [which is proportional to the population $P_{(39,35)}(t_1)$], and the intensity $I_2(t_1,t_2)$ of the second spike [which contains information about the feeding into state (39,35) from (40,36) between t_1 and t_2] follow the analytical functions,

$$I_1(t_1)=\varepsilon\left\{\frac{P^{(t=0)}_{(41,37)}\tau_{(41,37)}\tau_{(39,35)}\left(e^{-t_1/\tau_{(41,37)}}-e^{-t_1/\tau_{(40,36)}}\right)}{\left(\tau_{(41,37)}-\tau_{(40,36)}\right)\left(\tau_{(41,37)}-\tau_{(39,35)}\right)}+\left(P^{(t=0)}_{(40,36)}-\frac{P^{(t=0)}_{(41,37)}\tau_{(40,36)}}{\tau_{(41,37)}-\tau_{(40,36)}}\right)\frac{\tau_{(39,35)}\left(e^{-t_1/\tau_{(40,36)}}-e^{-t_1/\tau_{(39,35)}}\right)}{\tau_{(40,36)}-\tau_{(39,35)}}\right.$$
$$\left.+P^{(t=0)}_{(39,35)}e^{-t_1/\tau_{(39,35)}}\right\}, \tag{7a}$$

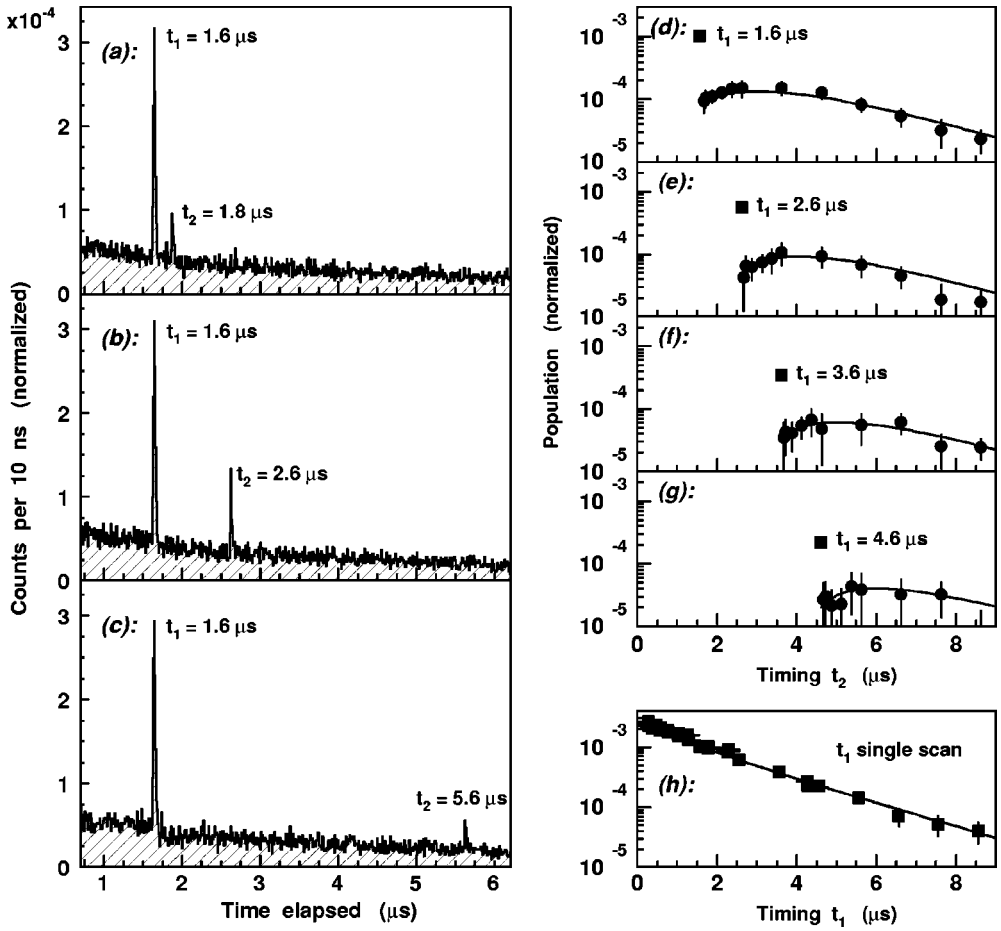

FIG. 11. Delayed annihilation time spectra measured by irradiating two successive laser pulses tuned to the transition $(n,\ell)=(39,35)\rightarrow(38,34)$ at wavelength $\lambda=597.3$ nm, the first laser fired at $t_1=1.6$ μs, the second laser at $t_2=1.8$ μs (a), 3.6 μs (b), and 5.6 μs (c). Time variations of the resonance intensities for cases where the first laser (closed squares) is fired at $t_1=1.6$ μs, and the second (closed circles) varied between $t_2=2.4$ and 9 μs (d); corresponding measurements made at a t_1 value of 2.6 μs (e), 3.6 μs (f), and 4.6 μs (g). Time variation of the resonance intensity was measured using a single laser pulse (h). Solid lines represent the best fit of a three-level cascade model.

$$
\begin{aligned}
I_2(t_1,t_2)=\varepsilon\Bigg\{&\frac{P^{(t=0)}_{(41,37)}\tau_{(41,37)}\tau_{(39,35)}e^{-t_2/\tau_{(41,37)}}\left(1-\varepsilon e^{-(1/\tau_{(39,35)}-1/\tau_{(41,37)})(t_2-t_1)}\right)}{(\tau_{(41,37)}-\tau_{(40,36)})(\tau_{(41,37)}-\tau_{(39,35)})}+P^{(t=0)}_{(39,35)}(1-\varepsilon)e^{-t_2/\tau_{(39,35)}}\\
&+\frac{P^{(t=0)}_{(41,37)}\tau_{(39,35)}\tau_{(40,36)}e^{-t_2/\tau_{(40,36)}}\left(1-\varepsilon e^{-(1/\tau_{(39,35)}-1/\tau_{(40,36)})(t_2-t_1)}\right)}{(\tau_{(40,36)}-\tau_{(41,37)})(\tau_{(40,36)}-\tau_{(39,35)})}+\frac{P^{(t=0)}_{(41,37)}\tau^2_{(39,35)}e^{-t_2/\tau_{(39,35)}}(1-\varepsilon)}{(\tau_{(39,35)}-\tau_{(41,37)})(\tau_{(39,35)}-\tau_{(40,36)})}\\
&+\frac{P^{(t=0)}_{(40,36)}\tau_{(39,35)}e^{-t_2/\tau_{(40,36)}}\{1-\varepsilon e^{-(1/\tau_{(39,35)}-1/\tau_{(40,36)})(t_2-t_1)}-(1-\varepsilon)e^{-(1/\tau_{(39,35)}-1/\tau_{(40,36)})t_2}\}}{\tau_{(40,36)}-\tau_{(39,35)}}\Bigg\}. \qquad (7b)
\end{aligned}
$$

The lifetime of state (39,35) was fixed to the experimental value $\tau_{(39,35)}=1.5$ μs [17]. The result of the best fit are shown with solid lines in Figs. 11(d)–11(h), and the deduced values of the state populations and lifetimes are presented in Table II. The estimated lifetime $\tau_{(40,36)}=(1.4\pm0.2)$ μs of (40,36) agrees with the theoretical radiative value [32] within the experimental errors. The primary populations of states (39,35), (40,36), and (41,37) were estimated to be $P_{(39,35)}(t=0)=(0.29\pm0.06)\%$, $P_{(40,36)}(t=0)=(0.06\pm0.02)\%$, and $P_{(41,37)}(t=0)=(0.03\pm0.02)\%$, respectively. States with $n\geqslant41$ apparently had very little metastable population. The measurement was repeated at a higher target density $\rho=1.2\times10^{21}$ cm^{-3} ($P=1.0$ bar, $T=6.4$ K), which yielded a similar result on the populations and lifetimes as shown in Table II.

TABLE II. Estimated lifetimes and populations of metastable states in the $v=3$ cascade at two target densities, derived from the best fit of a three-level cascade model. Theoretical radiative [22,32] and Auger [22,33] rates are shown.

Parameter	$P=0.5$ bar, $T=6.4$ K	$P=1.0$ bar, $T=6.4$ K	Theoretical radiative rate	Theoretical Auger rate
$\lambda_{(41,37)}$	$(0.5\pm0.3)\mu s^{-1}$	$(0.5\pm0.3)\ \mu s^{-1}$	0.48 μs^{-1} [22]	$<0.01\ \mu s^{-1}$ [22]
$\lambda_{(40,36)}$	$(0.52\pm0.18)\mu s^{-1}$	$(0.50\pm0.15)\mu s^{-1}$	0.55 μs^{-1} [32]	0.03 μs^{-1} [22]
$\lambda_{(39,35)}$	0.65 μs^{-1}[a]	$0.65\mu s^{-1}$[a]	0.62 μs^{-1} [32]	0.07 μs^{-1} [33]
$P_{(41,37)}$	$(0.03\pm0.02)\%$	$(0.02\pm0.01)\%$		
$P_{(40,36)}$	$(0.06\pm0.02)\%$	$(0.06\pm0.02)\%$		
$P_{(39,35)}$	$(0.29\pm0.06)\%$	$(0.27\pm0.05)\%$		

[a]Fixed to experimental value [17].

B. Population evolution of metastable states in the $v=2$ cascade

The population of state $(37,34)$ in the $v=2$ cascade was measured by inducing the transition $(37,34)\rightarrow(36,33)$ with a single laser pulse tuned to a wavelength $\lambda=470.7$ nm (Fig. 12). The time evolution contained several decay components,

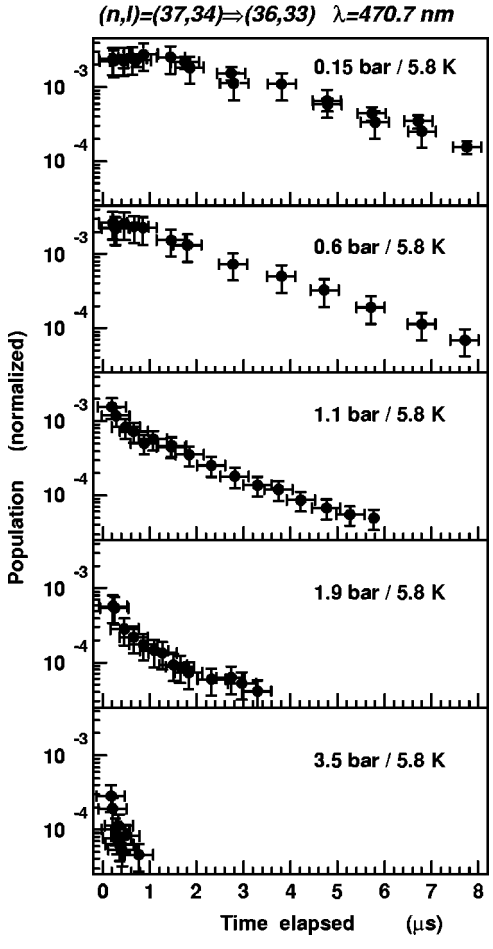

FIG. 12. The population evolution of state $(n,l)=(37,34)$ measured at five target densities, using the resonance transition $(37,34)\rightarrow(36,33)$ at wavelength $\lambda=470.7$ nm.

indicating that sizable populations exist in the higher states of the cascade: at a target density $\rho=1.9\times10^{20}$ cm^{-3} ($P=0.15$ bar, $T=5.8$ K), for example, the population decreased with an average lifetime $\tau_{avg}=3.0\pm0.1$ μs and had a downward-curving shape at early times. This indicates a large feeding of antiprotons from the higher state $(38,35)$. As the density was increased to $\rho=1.6\times10^{21}$ cm^{-3} ($P=1.1$ bar, $T=5.8$ K), however, the average lifetime decreased to $\tau_{avg}=1.8$ μs and a decay component with a lifetime $\tau_{short}=0.4$ μs appeared at early times in the spectrum. This indicates that the lifetime of $(37,34)$ was shortened due to collisional effects, in agreement with previous observations [17]. At a density $\rho=1.2\times10^{22}$ cm^{-3} ($P=3.5$ bar, $T=5.8$ K), the corresponding lifetimes shortened further to $\tau_{avg}<0.5$ μs and $\tau_{short}<0.2$ μs.

Next, the population in state $(38,35)$ was measured by using a double-resonance technique [16]. In Fig. 13(a), the annihilation spike of the 470.7-nm transition is shown, measured at density $\rho=1.9\times10^{21}$ cm^{-3} ($P=1.3$ bar, $T=5.8$ K), whereas in Fig. 13(b), the double-resonance transition $(38,35)\rightarrow(37,34)\rightarrow(36,33)$ induced by two simultaneous laser pulses tuned to the two transitions at wavelengths $\lambda_1=470.7$ nm and $\lambda_2=529.6$ nm is presented. The intensity of the spike in Fig. 13(b) constitutes a measure of the combined populations in two states $(38,35)$ and $(37,34)$, so that the population in the former state can be obtained by subtracting the contribution of the latter (Fig. 12). In Figs. 13(c)–(f), the population evolution of the two states measured at various target densities are shown. State $(38,35)$ had a primary population $P_{(38,35)}(t=0)=(0.49\pm0.08)\%$ which decayed with an average lifetime $\tau_{avg}=2.0\pm0.1$ μs, and these values were relatively unchanged at densities between $\rho=3\times10^{20}$ and 2×10^{21} cm^{-3}.

The lifetime of state $(38,35)$ was determined by using the depletion-recovery method [17]. In Fig. 14(a), the spectrum obtained by taking the difference between two delayed annihilation time spectra measured with and without the 470.7-nm annihilation spike is shown, measured at a density $\rho=1.9\times10^{21}$ cm^{-1} ($P=1.3$ bar, $T=5.8$ K). This depletion-recovery spectrum decays with the lifetime $\tau_{(36,33)}\sim4$ ns of the daughter state, the slight step-down discontinuity immediately after the spike caused by the loss of spontaneous

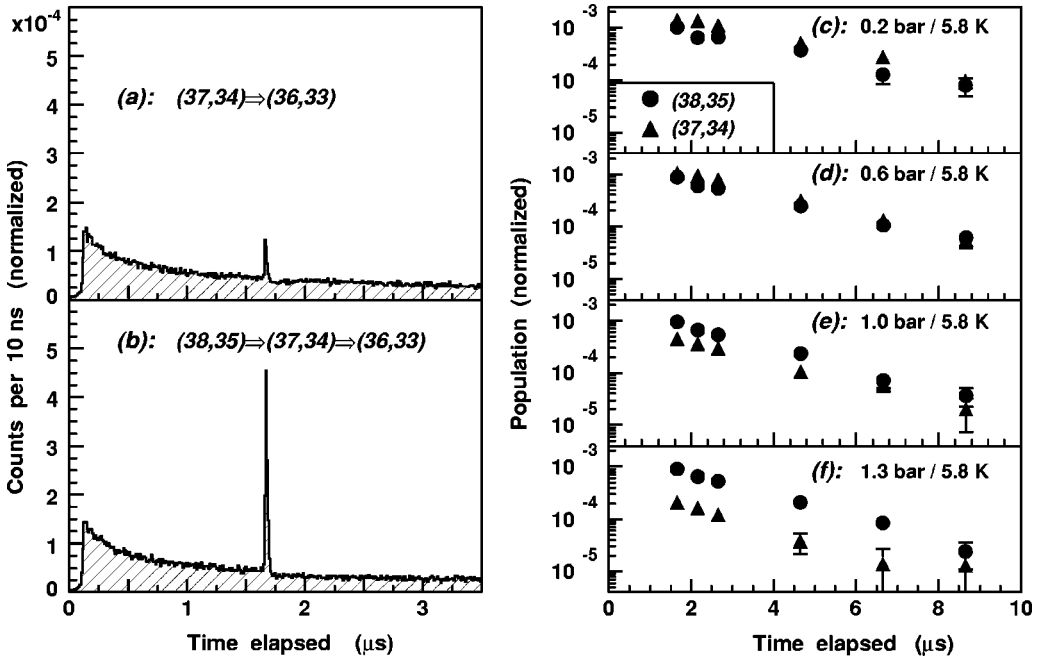

FIG. 13. The delayed annihilation time spectrum measured with a single laser pulse inducing the transition $(n,l)=(37,34)\rightarrow(36,33)$ at wavelength $\lambda=470.7$ nm (a). The double-resonance transition $(38,35)\rightarrow(37,34)\rightarrow(36,33)$ induced using two simultaneous laser pulses tuned to $\lambda_1=470.7$ nm and $\lambda_2=529.6$ nm (b). Both spectra were measured at a target pressure $P=1.3$ bar and temperature $T=5.8$ K. The population evolution of (38,35) (closed circles) and (37,34) (triangles) measured at four target densities (c)—(f).

annihilation events following the forced annihilation at the laser spike [17]. The spectrum then recovers with the lifetime $\tau_{(37,34)}\sim 0.2$ μs of the parent state. Since these characteristics are valid regardless of the various channels that feed antiprotons into the two levels, this method constitutes a sensitive and unambiguous way of determining the state lifetimes. Here we expand this method to the case of the double-resonance transition $(38,35)\rightarrow(37,34)\rightarrow(36,33)$, the depletion-recovery spectrum of which is shown in Fig. 14(b). Although the spectrum initially decayed with a lifetime similar to the single-resonance case [Fig. 14(a)], it recovered more slowly due to the long lifetime of state $(38,35)$. The spectrum can be understood by the relevant three-level decay model depicted in Fig. 15, where the radiative lifetimes of the states are denoted by $\tau^{\mathrm{rad}}_{(n,\ell)}$, and the feeding from adjacent states by $V_{(n,\ell)}$. The population evolution follows,

$$dP_{(38,35)}=\left(-\frac{P_{(38,35)}}{\tau_{(38,35)}}+V_{(38,35)}\right)dt, \tag{8a}$$

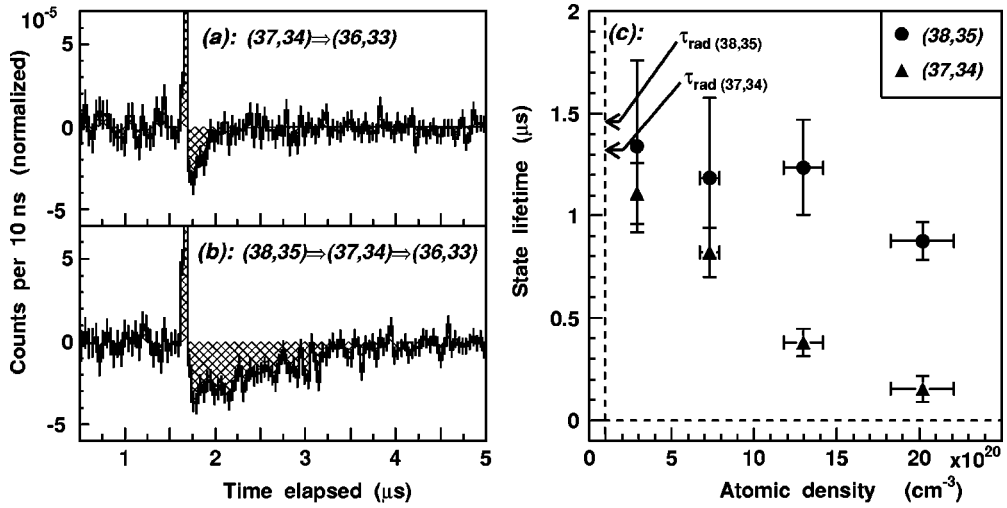

FIG. 14. The depletion-recovery spectrum of the transition $(n,l)=(38,35)\rightarrow(37,34)$ (a), and that of the double-resonance transition $(38,35)\rightarrow(37,34)\rightarrow(36,33)$ (b). Both spectra were measured at a target pressure $P=1.3$ bar and temperature $T=5.8$ K. The lifetimes of (38,35) (closed circles) and (37,34) (triangles) at various densities (c).

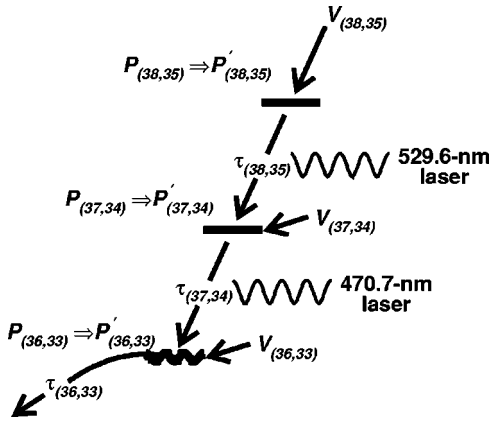

FIG. 15. The three-level cascade model. The populations in states $(n,l)=(38,35)$, (37,34) and (36,33) before laser irradiation are denoted by $P_{(38,35)}(t)$, $P_{(37,34)}(t)$, and $P_{(36,33)}(t)$; the feeding from the surrounding states by $V_{(n,l)}(t)$. The double-resonance transition induced by two simultaneous laser pulses at wavelengths $\lambda_1=470.7$ nm and $\lambda_2=529.6$ nm modify the state populations from $P_{(n,l)}(t)$ to $P'_{(n,l)}(t)$.

$$dP_{(37,34)} = \left(-\frac{P_{(37,34)}}{\tau_{(37,34)}} + \frac{P_{(38,35)}}{\tau_{(38,35)}} + V_{(37,34)} \right) dt, \qquad (8b)$$

$$dP_{(36,33)} = \left(-\frac{P_{(36,33)}}{\tau_{(36,33)}} + \frac{P_{(37,34)}}{\tau_{(37,34)}} + V_{(36,33)} \right) dt. \qquad (8c)$$

After the irradiation by the 470.7-nm and 529.6-nm laser pulses mix the populations in the three levels, the time evolution resumes the form implied by Eq. (8) with modified populations. Since the feeding from the surrounding states $(V_{(n,\ell)})$ are unaffected by the laser, the difference between the time spectra measured with and without the spike can be expressed in the form

$$P'_{(36,33)}(t) - P_{(36,33)}(t) = A_1 e^{-t/\tau_{(36,33)}} - A_2 e^{-t/\tau_{(37,34)}} - A_3 e^{-t/\tau_{(38,35)}}, \qquad (9)$$

where A_1, A_2, and A_3 are positive constants. The depletion-recovery spectrum implied by Eq. (9) therefore decays with the lifetime $\tau_{(36,33)}$ of the short-lived state and recovers with the combined lifetimes $\tau_{(37,34)}$ and $\tau_{(38,35)}$ of the two metastable ones. By fitting Eq. (9) on the depletion-recovery spectrum obtained from Fig. 14(b), and fixing the lifetimes of states (36,33) and (37,34) to their experimental values [17], the lifetime of (38,35) was determined as $\tau_{(38,35)}=(1.5\pm0.1)$ μs. In Fig. 14(c), the state lifetimes thus measured at four target densities are shown. The lifetime $\tau_{(38,35)}$ was relatively unchanged, having values 0.9–1.3 μs at densities between $\rho=3\times10^{20}$ and 2×10^{21} cm^{-3}, whereas $\tau_{(37,34)}$ shortened from (1.1 ± 0.2) to (0.15 ± 0.06) μs.

Lastly, the populations in state (39,35) and above in the $v=2$ cascade were estimated by irradiation with two successive laser pulses t_1 and t_2 tuned to the 470.7-nm transition. Measurements were made at three densities, $\rho=2\times10^{20}$ cm^{-3} ($P=0.2$ bar, $T=6.4$ K), 7×10^{20} cm^{-3} (0.6 bar, 6.4 K), and 1.2×10^{21} cm^{-3} (1.0 bar, 6.6 K), as shown in Fig. 16. In Table III and Fig. 16 (solid lines), the results of the best fit of a three-level cascade model on the data at each density are presented. The lifetime of state (37,34) was fixed to the experimentally measured value [17]. The primary populations in the three states at density $\rho=2\times10^{20}$ cm^{-3} were estimated to be $P_{(37,34)}=(0.21\pm0.08)\%$, $P_{(38,35)}=(0.40\pm0.10)\%$, and $P_{(39,36)}=(0.24\pm0.06)\%$. The populations were relatively unaffected as the density was increased from $\rho=2\times10^{20}$ to 1.2×10^{21} cm^{-3}, although the lifetime of state (37,34) decreased by an order of magnitude.

V. DISCUSSION

A. Primary populations

The primary populations in the $v=2$ and 3 cascades were relatively unaffected as the target density was increased from $\rho=2\times10^{20}$ to 1.2×10^{21} cm^{-3} (Tables II and III). The values for states (37,34), (38,35), (39,36), (39,35), (40,36), and (41,37) averaged over all the data measured at various densities were $P_{(37,34)}(t=0)=(0.21\pm0.04)\%$, $P_{(38,35)}(t=0)=(0.49\pm0.07)\%$, $P_{(39,36)}(t=0)=(0.19\pm0.07)\%$, $P_{(39,35)}(t=0)=(0.28\pm0.04)\%$, $P_{(40,36)}(t=0)=(0.06\pm0.02)\%$, and $P_{(41,37)}(t=0)=(0.02\pm0.01)\%$, respectively. The largest population was observed in state (38,35), which agrees with the estimation $n\sim n_0=38$ of Eq. (1). Using these results for calibration, a recent experiment [12] deduced the primary populations of nearly all the metastable states in both $\bar{p}^4\mathrm{He}^+$ and $\bar{p}^3\mathrm{He}^+$, thereby accounting for all the 3% metastability observed here (Fig. 7). Relatively little metastable populations were detected in states with $n\geqslant41$, whereas theoretical calculations [21–28] predict significant populations in states up to $n\geqslant50$. As these theoretical populations do not take the effect of collisions between $\bar{p}\mathrm{He}^+$ and helium atoms into account, however, they may not be directly comparable with the experimental results presented here which refer to atoms thermalized by many collisions. It has been suggested [54] that $\bar{p}\mathrm{He}^+$ created in the $n\geqslant41$ states recoil with such large kinetic energies that they are rapidly destroyed by collisions. Another study [55] suggests that the cross sections for collisional quenching of the $n\geqslant41$ states are large, even after the $\bar{p}\mathrm{He}^+$ atom has thermalized to the temperature ($T\sim6$ K) of the gas target. This is claimed to be due to the low activation barrier in the $\bar{p}^4\mathrm{He}^+-\mathrm{He}$ potential.

B. Density-dependent shortening of the state lifetimes

It is surprising that these atoms retain their metastability in dense gas, liquid, and superfluid helium targets, despite making many collisions with the surrounding helium atoms. Stark transitions induced by collisional effects, which destroy other types of antiprotonic atoms [56,57], are believed to be highly suppressed in $\bar{p}\mathrm{He}^+$; this is because states of the same n-value are far from degenerate, the level energies increasing with ℓ in steps of $E_{(n,\ell)}-E_{(n,\ell-1)}\sim0.3$ eV (Fig. 1). Recently, a quantitative study of these transitions has been made [58].

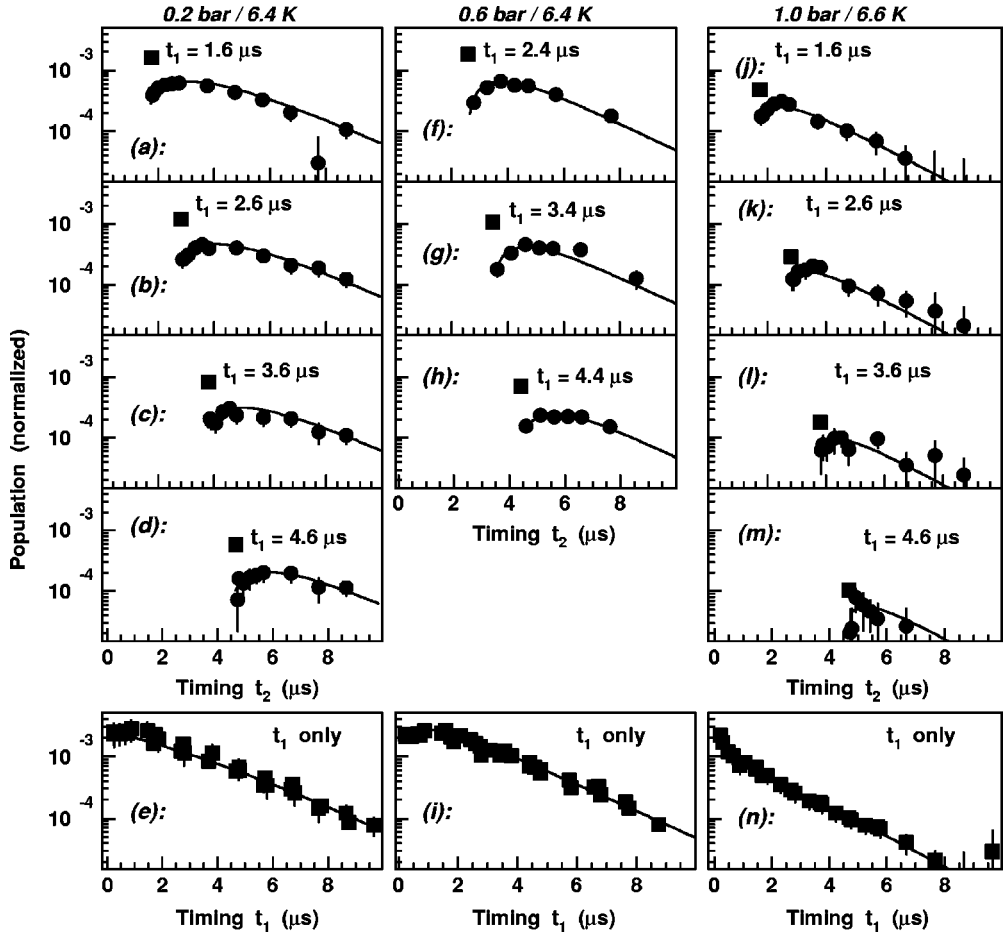

FIG. 16. Time-variation of the intensity of the resonance transition $(n,l)=(37,34)\rightarrow(36,33)$ measured using two laser pulses fired at timing t_1 (closed squares) and t_2 (closed circles) tuned to wavelength $\lambda=470.7$ nm. Measurements were made at three target conditions: $P=0.2$ bar, $T=6.4$ K [(a)-(e)], $P=0.6$ bar, $T=6.4$ K [(f)-(i)], and $P=1.0$ bar, $T=6.6$ K [(j)-(n)]. The results of the best fit of a three-level cascade model are shown in solid lines.

The present experiment and previous studies [17] show that even after thermalization, collisions with helium atoms continue to destroy the population in state (37,34), while they leave the higher states (38,35) and (39,35) relatively unaffected. The decay rate of (37,34) increased non-linearly with density, from the purely radiative value $1/\tau_{(37,34)}=0.8\ \mu s^{-1}$ observed at $\rho=1\times10^{20}\ cm^{-3}$, to $\sim8\ \mu s^{-1}$ at $3\times10^{21}\ cm^{-3}$, then leveled off at higher densities. State (39,35), however, retained the radiative rate $1/\tau_{(39,35)}=0.7\ \mu s^{-1}$ even at liquid-helium densities, while (38,35) maintained a decay rate $1/\tau_{(38,35)}\sim1\ \mu s^{-1}$ at densities up to $\rho=2\times10^{21}\ cm^{-1}$.

TABLE III. Estimated lifetimes and populations of metastable states in the $v=2$ cascade at three target densities, derived from the best fit of a three-level cascade model. Theoretical radiative [32] and Auger [22,33] rates are shown.

Parameter	$P=0.2$ bar, $T=6.4$ K	$P=0.6$ bar, $T=6.4$ K	$P=1.0$ bar, $T=6.6$ K	Theoretical radiative rate	Theoretical Auger rate
$\lambda_{(39,36)}$	$(0.6\pm0.1)\mu s^{-1}$	$(0.6\pm0.2)\ \mu s^{-1}$	$(0.6\pm0.2)\ \mu s^{-1}$	$0.62\ \mu s^{-1}$ [32]	$<0.01\ \mu s^{-1}$ [22]
$\lambda_{(38,35)}$	$(0.6\pm0.1)\mu s^{-1}$	$(0.6\pm0.1)\mu s^{-1}$	$(0.7\pm0.2)\mu s^{-1}$	$0.69\ \mu s^{-1}$ [32]	$0.011\ \mu s^{-1}$ [33]
$\lambda_{(37,34)}$	$0.85\ \mu s^{-1}$[a]	$1.3\ \mu s^{-1}$[a]	$1.9\ \mu s^{-1}$[a]	$0.76\ \mu s^{-1}$ [32]	$0.19\ \mu s^{-1}$ [33]
$P_{(39,36)}$	$(0.21\pm0.08)\%$	$(0.25\pm0.09)\%$	$(0.14\pm0.07)\%$		
$P_{(38,35)}$	$(0.04\pm0.10)\%$	$(0.55\pm0.08)\%$	$(0.40\pm0.20)\%$		
$P_{(37,34)}$	$(0.24\pm0.06)\%$	$(0.20\pm0.04)\%$	$(0.26\pm0.10)\%$		

[a]Fixed to experimental value [17].

At a target density $\rho=2\times10^{20}$ cm^{-3}, the primary population $P_{(37,34)}(t=0)=(0.21\pm0.04)\%$ of state $(37,34)$ decreased with an average lifetime $\tau_{\mathrm{avg}}\sim3$ μs (Fig. 12), while at $\rho=1.2\times10^{21}$ cm^{-3}, the lifetime shortened to $\tau_{\mathrm{avg}}<0.5$ μs. A similar shortening behavior was observed at early times in the delayed annihilation time spectrum (Fig. 6), which reflects the overall lifetime of $\bar{p}\mathrm{He}^+$ against annihilation. As the target density was increased from $\rho=6\times10^{20}$ to 2×10^{22} cm^{-3}, a short-lived component with a $\sim0.2-\mu$s lifetime appeared, while the total fraction of atoms surviving more than $t=20$ ns decreased from $f_{\mathrm{trap}}=3.0$ to 2.5%. This similarity implies that the above short-lived component and the reduction of the metastable population at high target densities are partially caused by the lifetime-shortening of state $(37,34)$.

VI. SUMMARY AND CONCLUSIONS

We have developed a laser spectroscopic method to determine the absolute number of antiprotons populating individual states (n,ℓ) of the $\bar{p}\mathrm{He}^+$ atom. By evaluating all known sources of experimental error and background (such as the probability of an antiproton stopping in the volume of the helium target irradiated by the laser beam, spurious signals caused by the in-flight nuclear reaction of antiprotons, the non-unity efficiency of a resonant laser pulse inducing an atomic transition leading to antiproton annihilation, and the background caused by $\pi^+\rightarrow\mu^+\rightarrow e^+$ decay), the primary populations $P_{(n,\ell)}(t=0)$ were determined with experimental errors of 20–70%. To our knowledge, this constitutes the most precise measurement of the values $P_{(n,\ell)}(t=0)$ of an exotic atom (i.e., an atom wherein an electron is replaced by a negatively charged particle such as a π^-, K^-, or $\bar{p}$). Metastable states in the $n=37-40$ and $\ell=34-36$ region each contained $P_{(n,\ell)}(t=0)=0.1-0.5\%$ of the antiprotons stopped in the helium target, whereas the $n\geqslant41$ region contained relatively little metastable population. The population in state $(n,\ell)=(37,34)$ was destroyed by collisions with helium atoms at high target densities (the average lifetime of its population decreasing from $\tau_{\mathrm{avg}}=3$ to <0.5 μs as the atomic density was increased from $\rho=2\times10^{20}$ to 1.2×10^{22} cm^{-3}), while the lifetimes of two other states $(39,35)$ and $(38,35)$ remained relatively unchanged. This behavior of the individual states affected the overall lifetime of $\bar{p}\mathrm{He}^+$ against annihilation: as the target density was increased from $\rho=6\times10^{20}$ to 2×10^{22} cm^{-3}, a short-lived component appeared at early times in the delayed annihilation time spectrum, while the yield of metastable atoms decreased from 3.0 to 2.5%. The primary populations derived here will be used to normalize the results of a new series of experiments [12,59,60] carried out at the AD.

ACKNOWLEDGMENTS

We are indebted to the CERN Proton Synchrotron division for providing a stable antiproton beam, and to the cryogenics laboratory for their help in manufacturing the helium target. The present work was supported by the Grants-in-Aid for Specially Promoted Research and for International Scientific Research of Monbukagakusho of Japan, the German Bundesministerium für Bildung, Wissenschaft, Forschung und Technologie, and the Hungarian National Science Foundation (T033079).

[1] M. Iwasaki, S. N. Nakamura, K. Shigaki, Y. Shimizu, H. Tamura, T. Ishikawa, R. S. Hayano, E. Takada, E. Widmann, H. Outa, M. Aoki, P. Kitching, and T. Yamazaki, Phys. Rev. Lett. **67**, 1246 (1991).

[2] T. Yamazaki, E. Widmann, R. S. Hayano, M. Iwasaki, S. N. Nakamura, K. Shigaki, F. J. Hartmann, H. Daniel, T. von Egidy, P. Hofmann, Y.-S. Kim, and J. Eades, Nature (London) **361**, 238 (1993).

[3] T. Yamazaki, N. Morita, R. S. Hayano, E. Widmann, and J. Eades, Phys. Rep. **366**, 183 (2002).

[4] S. N. Nakamura, R. S. Hayano, M. Iwasaki, K. Shigaki, E. Widmann, T. Yamazaki, H. Daniel, T. von Egidy, F. J. Hartmann, P. Hofmann, Y.-S. Kim, and J. Eades, Phys. Rev. A **49**, 4457 (1994).

[5] E. Widmann, I. Sugai, T. Yamazaki, R. S. Hayano, M. Iwasaki, S. N. Nakamura, H. Tamura, T. M. Ito, A. Kawachi, N. Nishida, W. Higemoto, Y. Ito, N. Morita, F. J. Hartmann, H. Daniel, T. von Egidy, W. Schmid, J. Hoffmann, and J. Eades, Phys. Rev. A **51**, 2870 (1995).

[6] B. Ketzer, F. J. Hartmann, H. Daniel, T. von Egidy, A. Nieстroj, S. Schmid, W. Schmid, T. Yamazaki, I. Sugai, K. Nakayoshi, R. S. Hayano, F. E. Maas, H. A. Torii, T. Ishikawa, H. Tamura, N. Morita, D. Horváth, J. Eades, and E. Widmann, Phys. Rev. A **53**, 2108 (1996).

[7] G. T. Condo, Phys. Lett. **9**, 65 (1964).

[8] J. E. Russell, Phys. Rev. Lett. **23**, 63 (1969); Phys. Rev. **188**, 187 (1969); Phys. Rev. A **1**, 721 (1970); **1**, 735 (1970); **1**, 742 (1970); J. Math. Phys. **12**, 1906 (1971); Phys. Rev. A **6**, 2488 (1972).

[9] S. Baird, J. Bosser, M. Chanel, P. Lefévre, R. Ley, D. Manglunki, S. Maury, D. Möhl, and G. Tranquille, Hyperfine Interact. **76**, 61 (1993).

[10] M. Chanel, *LEAR Performance*, Proceedings of the LEAR Symposium, CERN, Geneva, 1998, CERN/PS 99-040, (CERN, Geneva, 1999).

[11] M. Hori, J. Eades, R. S. Hayano, T. Ishikawa, J. Sakaguchi, E. Widmann, H. Yamaguchi, H. A. Torii, B. Juhász, D. Horváth, and T. Yamazaki, Phys. Rev. Lett. **87**, 093401 (2001).

[12] M. Hori, J. Eades, R. S. Hayano, T. Ishikawa, J. Sakaguchi, T. Tasaki, E. Widmann, H. Yamaguchi, H. A. Torii, B. Juhász, D. Horváth, and T. Yamazaki, Phys. Rev. Lett. **89**, 093401 (2002).

[13] N. Morita, M. Kumakura, T. Yamazaki, E. Widmann, H. Masuda, I. Sugai, R. S. Hayano, F. E. Maas, H. A. Torii, F. J. Hartmann, H. Daniel, T. von Egidy, B. Ketzer, W. Müller, W. Schmid, D. Horváth, and J. Eades, Phys. Rev. Lett. **72**, 1180

(1994).
[14] R. S. Hayano, F. E. Maas, H. A. Torii, N. Morita, M. Kumakura, T. Yamazaki, H. Masuda, I. Sugai, F. J. Hartmann, H. Daniel, T. von Egidy, B. Ketzer, W. Müller, W. Schmid, D. Horváth, J. Eades, and E. Widmann, Phys. Rev. Lett. **73**, 1485 (1994); **73**, 3181(E) (1994).
[15] F. E. Maas, R. S. Hayano, T. Ishikawa, H. Tamura, H. A. Torii, N. Morita, T. Yamazaki, I. Sugai, K. Nakayoshi, F. J. Hartmann, H. Daniel, T. von Egidy, B. Ketzer, A. Niestroj, S. Schmid, W. Schmid, D. Horváth, J. Eades, and E. Widmann, Phys. Rev. A **52**, 4266 (1995).
[16] R. S. Hayano, T. Ishikawa, H. Tamura, H. A. Torii, M. Hori, F. E. Maas, N. Morita, M. Kumakura, I. Sugai, F. J. Hartmann, H. Daniel, T. von Egidy, B. Ketzer, R. Pohl, D. Horváth, J. Eades, E. Widmann, and T. Yamazaki, Phys. Rev. A **55**, R1 (1997).
[17] M. Hori, H. A. Torii, R. S. Hayano, T. Ishikawa, F. E. Maas, H. Tamura, B. Ketzer, F. J. Hartmann, R. Pohl, C. Maierl, M. Hasinoff, T. von Egidy, M. Kumakura, N. Morita, I. Sugai, D. Horváth, E. Widmann, J. Eades, and T. Yamazaki, Phys. Rev. A **57**, 1698 (1998); **58**, 1612(E) (1998).
[18] F. J. Hartmann, B. Ketzer, C. Maierl, R. Pohl, T. von Egidy, R. S. Hayano, M. Hori, T. Ishikawa, H. Tamura, H. A. Torii, M. Kumakura, N. Morita, I. Sugai, D. Horváth, J. Eades, E. Widmann, and T. Yamazaki, Phys. Rev. A **58**, 3604 (1998).
[19] H. A. Torii, R. S. Hayano, M. Hori, T. Ishikawa, N. Morita, M. Kumakura, I. Sugai, T. Yamazaki, B. Ketzer, F. J. Hartmann, T. von Egidy, R. Pohl, C. Maierl, D. Horváth, J. Eades, and E. Widmann, Phys. Rev. A **59**, 223 (1999).
[20] A review is given in F. J. Hartmann, *Electromagnetic Cascade and Chemistry of Exotic Atoms* (Plenum Press, New York, 1990), pp. 23–39; 127–139.
[21] J. S. Cohen, R. L. Martin, and W. R. Wadt, Phys. Rev. A **27**, 1821 (1983).
[22] K. Ohtsuki (private communication).
[23] V. K. Dolinov, G. Ya. Korenman, I. V. Moskalenko, and V. P. Popov, Muon Catal. Fusion **4**, 169 (1989).
[24] G. Ya. Korenman, Hyperfine Interact. **101-102**, 81 (1996); Nucl. Phys. A **A692**, 145c (2001).
[25] W. A. Beck, L. Wilets, and M. A. Alberg, Phys. Rev. A **48**, 2779 (1993); private communication.
[26] J. S. Briggs, P. T. Greenland, and E. A. Solov'ev, J. Phys. B **32**, 197 (1999).
[27] J. S. Cohen, Phys. Rev. A **62**, 022512 (2000).
[28] K. Tökési, in International Conference on Low Energy Antiproton Physics, Yokohama, 2003 (unpublished).
[29] R. Ahlrichs, O. Dumbrajs, H. Pilkuhn, and H. G. Schlaile, Z. Phys. A **306**, 297 (1982).
[30] T. Yamazaki and K. Ohtsuki, Phys. Rev. A **45**, 7782 (1992).
[31] I. Shimamura, Phys. Rev. A **46**, 3776 (1992).
[32] P. T. Greenland and R. Thürwächter, Hyperfine Interact. **76**, 355 (1993).
[33] V. I. Korobov and I. Shimamura, Phys. Rev. A **76**, 4587 (1997).
[34] T. B. Day, Nuovo Cimento **18**, 381 (1960).
[35] G. Reifenröther, E. Klempt, and R. Landua, Phys. Lett. B **203**, 9 (1988).
[36] M. Hori, K. Yamashita, R. S. Hayano, and T. Yamazaki, Nucl. Instrum. Methods Phys. Res. A **496**, 102 (2003).
[37] M. Hori, Nucl. Instrum. Methods Phys. Res. A **522**, 420 (2004).
[38] Particle Data Group, K. Hagiwara *et al.*, Phys. Rev. D **66**, 010001 (2002).
[39] C. J. Batty, E. Friedman, and A. Gal, Phys. Rep. **287**, 385 (1997).
[40] H. A. Torii, R. S. Hayano, F. E. Maas, N. Morita, M. Kumakura, T. Yamazaki, H. Masuda, I. Sugai, B. Ketzer, F. J. Hartmann, H. Daniel, T. von Egidy, W. Müller, W. Schmid, D. Horváth, J. Eades, and E. Widmann, Nucl. Instrum. Methods Phys. Res. A **396**, 257 (1997).
[41] J. F. Ziegler, J. P. Biersack, and U. Littmark, *The Stopping and Range of Ions in Solids* (Pergamon, New York, 1985).
[42] M. Agnello *et al.*, Phys. Rev. Lett. **74**, 371 (1995).
[43] A. Zenoni *et al.*, Phys. Lett. B **B461**, 405 (1999).
[44] J. Carbonell, K. V. Protasov, and A. Zenoni, Phys. Lett. B **B397**, 345 (1997).
[45] K. V. Protasov, G. Bonomi, E. Lodi Rizzini, and A. Zenoni, Eur. Phys. J. A **7**, 429 (2000).
[46] A. Zenoni *et al.*, Phys. Lett. B **B461**, 413 (1999).
[47] C. J. Batty, E. Friedman, and A. Gal, Nucl. Phys. A **A689**, 721 (2001).
[48] A. Gal, E. Friedman, and C. J. Batty, Phys. Lett. B **B491**, 219 (2000).
[49] A. Bianconi *et al.*, Phys. Lett. B **B481**, 194 (2000).
[50] F. Balestra *et al.*, Nucl. Instrum. Methods Phys. Res. A **A452**, 573 (1986).
[51] S. N. Nakamura, doctoral thesis, University of Tokyo, 1995 (unpublished).
[52] S. Agostinelli *et al.*, Nucl. Instrum. Methods Phys. Res. A **506**, 250 (2003).
[53] G. Bendiscioli *et al.*, Nucl. Phys. A **A518**, 683 (1990).
[54] G. Ya. Korenman, Phys. At. Nucl. **59**, 1665 (1996).
[55] S. Sauge and P. Valiron, Chem. Phys. **265**, 47 (2001).
[56] T. B. Day, G. A. Snow, and J. Sucher, Phys. Rev. Lett. **3**, 61 (1959).
[57] M. Leon and H. A. Bethe, Phys. Rev. **127**, 636 (1962).
[58] J. E. Russell, Phys. Rev. A **65**, 032509 (2002); **65**, 069904(E) (2002).
[59] M. Hori, J. Eades, R. S. Hayano, T. Ishikawa, W. Pirkl, E. Widmann, H. Yamaguchi, H. A. Torii, B. Juhász, D. Horváth, and T. Yamazaki, Phys. Rev. Lett. **91**, 123401 (2003).
[60] M. Hori, R. S. Hayano, E. Widmann, and H. A. Torii, Opt. Lett. **28**, 2479 (2003).